Originally published as:

# A numerical approach for modelling fault-zone trapped waves

A.K. Gulley,[1] J.P. Kaipio,[1,2] J.D. Eccles[3] and P.E. Malin[4,5]

[1]*Department of Mathematics and Dodd-Walls Centre, University of Auckland, Private Bag* 92019, 1142 *Auckland, New Zealand.*
*E-mail:* anton.gulley@auckland.ac.nz
[2]*Department of Applied Physics, University of Eastern Finland, P.O. Box* 1627, *FI-*70211 *Kuopio, Finland*
[3]*School of Environment, University of Auckland, Private Bag* 92019, 1142 *Auckland, New Zealand*
[4]*Department of Physics, University of Auckland, Private Bag* 92019, 1142 *Auckland, New Zealand*
[5]*GFZ German Research Center for Geosciences, Telegrafenberg, D-*14473 *Potsdam, Germany*

## SUMMARY

We develop a computationally efficient approach to compute the waveforms and the dispersion curves for fault-zone trapped waves guided by arbitrary transversely isotropic across-fault velocity models. The approach is based on a Green's function type representation for $F_L$ and $F_R$ type fault-zone trapped waves. The model can be used for simulation of the waveforms generated by both infinite line sources (2-D) and point sources (3-D). The numerical scheme is based on a high order finite element approximation and, to increase computational efficiency, we make use of absorbing boundary conditions and mass lumping of finite element matrices.

**Key words:** Numerical approximations and analysis; Numerical solutions; Guided waves; Seismic anisotropy.

## 1 INTRODUCTION

A mature fault zone represents a significant zone of weakness within the earth's crust that accommodates focussed crustal strain as active earthquake rupture, slow slip or creep (Peng & Gomberg 2010). Characteristics such as fracturing, brecciation, remineralization and high pore-fluid pressure in the fault often result in lower bulk seismic velocities than in the surrounding country-rock (Mooney & Ginzburg 1986; Chester *et al.* 1993; Cochran *et al.* 2009).

Fault-zone trapped (or guided) waves (FZTWs) are seismic waves that travel in the low velocity region of a fault zone (Li *et al.* 2012). These waves are characterized by being at least partially trapped or guided in the fault zone through internal reflections off the higher velocity country-rock. The FZTWs have many similar properties to surface waves and there are FZTWs that correspond to the Love, Rayleigh and leaky surface wave types. The $F_L$ FZTWs are analogous to Love mode surface waves and have fault-parallel polarization (*SH* motion, Li *et al.* 2012). The observation of $F_L$ phases on an active fault were first reported from controlled source surface-to-borehole studies at Oroville, California (Leary *et al.* 1985, 1987; Li & Leary 1990; Li *et al.* 1990). The $F_R$ FZTWs are analogous to Rayleigh mode surface waves and have radial and fault orthogonal polarization (PSV motion). The $F_\phi$ phases are a leaky FZTW type that arrive between the *P*- and *S*-wave first arrivals and are only partially trapped by the waveguide. The $F_R$ and leaky ($F_\phi$) FZTWs were first identified in passive source experiments on the San Andreas Fault (Malin & Lou 1996; Ellsworth & Malin 2011).

FZTWs are dispersive body waves. The $F_R$ and $F_L$ waves arrive after the *S*-wave and typically have a higher amplitude after significant propagation distances (Huang *et al.* 1995). The amplitude and frequency content of FZTWs depend strongly on the physical properties and geometry of the fault zone and the surrounding rock (Li & Vidale 1996; Ben-Zion 1998; Igel *et al.* 2002). Modelling of FZTWs has therefore been used to estimate the elastic properties and geometry of a fault zone at a resolution of tens to hundreds of metres (Ben-Zion *et al.* 1992, 2003; Hough *et al.* 1994; Li *et al.* 1990, 1997, 1998, 1999, 2014; Li & Vernon 2001; Haberland *et al.* 2003, 2007; Mizuno *et al.* 2004; Lewis *et al.* 2005, 2007; Li & Malin 2008; Wu *et al.* 2010; Ellsworth & Malin 2011; Eccles *et al.* 2015).

Modelling of FZTWs can be broadly categorized in to two types. These two methodologies are numerical full waveform solvers and semi-analytic trapped wave solvers.

The numerical full waveform solvers that are used in FZTW investigations are typically 2-D or 3-D finite difference approaches (e.g. Graves 1996). These numerical approaches output the entire wave field produced by a source including the FZTW. Full waveform solvers allow investigations into the properties of FZTWs as influenced by different velocity models or source types and locations (Li & Vidale 1996; Igel *et al.* 1997, 2002; Jahnke *et al.* 2006). The computationally intensive 3-D full waveform solvers have also been used for the estimation of fault zone parameters through forward modelling (Li *et al.* 2000, 2003, 2014; Mamada *et al.* 2002, 2004; Mizuno *et al.* 2004; Li & Malin 2008). The high computational time (hours) means that full waveform solvers are generally impractical for estimating fault zone parameters through inversion which requires many evaluations of the forward model.

There are several different types of semi-analytic trapped wave solvers. The simplest is the fully analytic solution to $F_L$ in a homogenous fault-zone sandwiched by homogenous higher velocity country-rock (Li & Leary 1990; Ben-Zion 1998; Li *et al.* 2012). Other approaches include the generalization of surface wave methods such as propagator matrix methods (e.g. Malin & Lou 1996).

These methods are sufficiently computationally fast for inversion and have been previously used in this way (Haberland *et al.* 2003, 2007; Wu *et al.* 2010; Wu & Hole 2011). These methods are limited to 1-D stratified velocity models which may poorly represent real world geologic complexity (Faulkner *et al.* 2010).

The described limitation of these semi-analytic trapped wave solvers means that many of the inversions performed to date assume that the fault zone is a single homogenous layer surrounded by homogenous country-rock (Malin & Lou 1996; Wu & Hole 2011). Many fault zones, however, have gradational boundaries (Leary *et al.* 1987), which is shown to significantly affect the dispersion characteristics of the trapped wave in Gulley *et al.* (2017).

It is also expected that many fault zones have bulk anisotropic elastic properties (Leary *et al.* 1987; Li *et al.* 1987; Cochran & Vidale 2001). This anisotropy could be caused by parallel layering of fault rocks or juxtaposed geology, preferential alignment of fractures or other intrinsic rock properties such as crystal orientation and type. In some cases this anisotropic elastic velocity profile can be well approximated by a transversely isotropic velocity model (Leary *et al.* 1987; Li *et al.* 1987). In this paper transverse-isotropy in fault-zones means that any wave travelling parallel to the central fault plane has the same velocity, but the velocities change if the wave direction has a component normal to the fault plane. Anisotropy in coal seam waveguides has been well explored (Buchanan *et al.* 1983). A methodology for modelling guided waves with arbitrary fracture orientation was developed by Lou & Crampin (1991). This methodology assumes the waveguide is made up of several homogeneous anisotropic layers and uses layer matching techniques. It is shown in Lou & Crampin (1991) that guided waves in anisotropic waveguides have similar properties to those in isotropic waveguides however anisotropy does cause variations in group velocities. These variations may be important if guided waves are being used to image waveguides.

In this paper, we derive a semi-analytical computational model for $F_L$ and $F_R$ type FZTWs that propagate in 3-D. The velocity model is restricted to wave variations in the across-fault direction only (1-D) and it has fault-parallel transverse-isotropy. This model has two aims. The first is to develop a model that attempts to allow for a velocity structure with gradational boundaries and anisotropy but is sufficiently efficient such that it could be employed in the inversion. The second is to compute Green's function type representations (amplitude response) for FZTW from a point source with an arbitrary 1-D velocity model. Such a representation of the amplitude response and dispersion curves allows for further analysis of FZTW. This analysis could include understanding which properties of the waveguide or earthquake have the most significant effect on the amplitude or dispersion of particular frequencies; and such an analysis would be difficult if only modelling the coda in the time domain.

The present paper focuses on developing the numerical method and improving computational efficiency. Synthetic investigations using the model, including investigating anisotropy and gradational velocity models, are presented in a sister paper (Gulley *et al.* 2017).

# 2 A NUMERICAL APPROACH TO COMPUTE FZTWs GENERATED BY AN ARBITRARY 1-D VELOCITY MODEL

## 2.1 Overview of the approach

We developed a numerical and computational scheme to compute the trapped frequencies and waveforms of the $F_L$ and $F_R$ FZTWs with a transversely isotropic velocity model that allowed for arbitrary velocity variations in the direction across-fault. The numerical approach was based on a high order finite element method because of its high computational efficiency (Wiggins 1976). The finite element method also has an advantage over approaches such as matrix propagator methods (e.g. Thomson 1950; Haskell 1953) or layer matching methods (Li & Leary 1990; Ben-Zion 1998; Li *et al.* 2012) as it allows for the elastic properties to be varied over an element, thus reducing the number of points needed to approximate complex velocity models. On the truncation boundary of the computational domain, we employed absorbing boundary conditions. Further computational speed was gained by the use of a mass lumping approximation (Cohen *et al.* 1993), which reduces the complexity of the eigenvalue problem.

Once the trapped modes and dispersion curves of the FZTWs have been calculated, we use a generalization of the equations in Aki & Richards (2009, section 7.2) for transversely isotropic trapped waves to calculate the Green's function (amplitude response) as Li & Leary (1990) and Li *et al.* (2012) did for $F_L$. This allows the FZTW waveform to be computed efficiently for multiple different source types. These source types include infinite line sources (2-D wave propagation) and moment tensor point sources (3-D wave propagation from an earthquake).

The capabilities of this approach are shown in Fig. 1. In this figure, an example velocity model with gradational boundaries consistent with decreasing fracture density with distance from the fault core (Faulkner *et al.* 2010) provides the waveguide. The FZTWs are generated from a strike slip earthquake occurring at 3 km depth and 3 km along strike from the receiver. Dispersion curves, Green's function (amplitude response) and the associated FZTW waveform are shown.

## 2.2 Anisotropic propagation in a waveguide

We derive the equations and solutions for a FZTW with an arbitrary transversely isotropic velocity model in which the velocity varies only in the direction (denoted by $z$ below) across the fault. The notations and the general approach largely follows the treatment of surface waves in Aki & Richards (2009), which we generalize here for transversely isotropic trapped waves. We assume that the FZTW propagates in the $x$ direction. The plane wave solution to the full elastic wave equation can be written as

$$\mathbf{u}(x, z, \omega, k, t) = r_1(k, z, \omega) \exp(i(kx - \omega t))\hat{\mathbf{x}}$$
$$+ i r_2(k, z, \omega) \exp(i(kx - \omega t))\hat{\mathbf{z}}$$
$$+ l(k, z, \omega) \exp(i(kx - \omega t))\hat{\mathbf{y}}, \tag{1}$$

where $i = \sqrt{-1}$ is the imaginary unit and is introduced in the $\hat{\mathbf{z}}$ term to make the $r_1$ and $r_2$ components in-phase with each other. The unit vector in the direction across the fault is $\hat{\mathbf{z}}$ and $\hat{\mathbf{x}}$, $\hat{\mathbf{y}}$ are the two remaining unit vectors in the right hand coordinate system. The angular frequency is $\omega$, $k$ is the wave number in the $x$ direction and the phase speed is $c = \omega/k$.

We take the transverse-isotropy planes of symmetry to be the $z =$ constant (fault-parallel) planes and thus, without loss of generality, we will only consider the $x$ and $z$ directions. We define the propagation angle $\theta$ that describes wave propagation direction in the $x$–$z$ plane with $\theta = 0°$, meaning propagation in the fault-perpendicular $z$ direction, and $\theta = 90°$ referring to propagation in the fault-parallel $x$ direction as seen in Fig. 2. The elastic tensor coefficients $C_{ij}$ and the density $\rho$ are functions of $z$ only. A
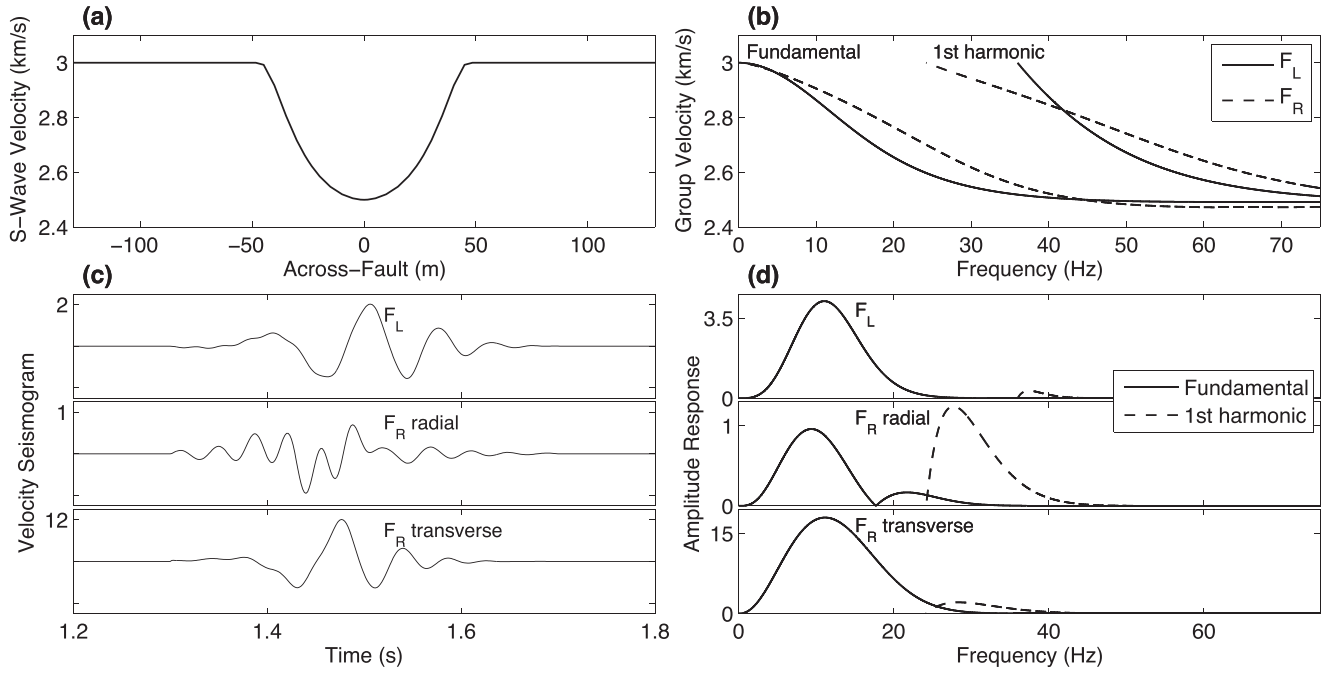
**Figure 1.** Example outputs from proposed finite element fault-zone trapped wave modelling methodology. (a) *S*-wave velocity model. The *P*-wave velocity and the density have a similar shape to the *S*-wave velocity but with ranges of 5–5.3 km s$^{-1}$ and 2.6–2.7 g cm$^{-3}$ respectively. Isotropy is assumed. The *P*-wave (attenuation) $Q$ factor has the same profile with a range of 20–100 and the *S*-wave $Q$ factor has a range of 10–50. (b) Dispersion curves of the fundamental and first harmonics. (c) FZTW waveforms produced from a purely strike slip earthquake in a vertically oriented fault that is located at 3 km depth and 3 km along the strike from the receiver. The source and receiver are located 25 m from the central fault plane, the source spectrum used is 1/frequency and only the fundamental and first harmonic is used. The numbers on the axis show the relative amplitudes of the waveforms. (d) The Green's function (amplitude response) that, together with the dispersion curve, produced the waveforms seen in (c). The numbers on the axis show the relative amplitudes of the waveforms.
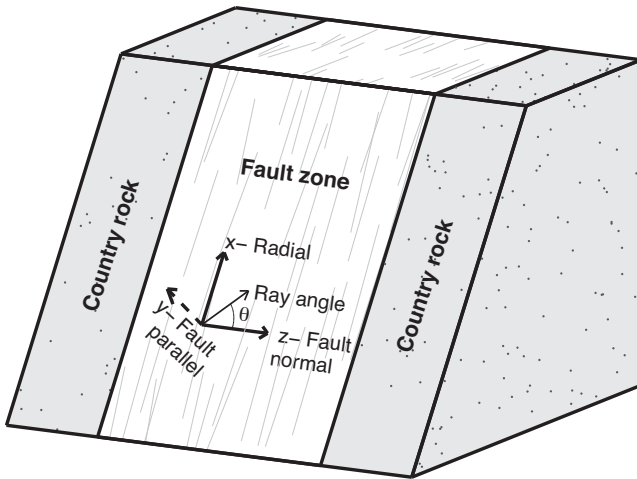


**Figure 2.** The coordinate system used. An individual wave ray is travelling in the direction described by the 'ray angle' but due to the waveguide the FZTW net energy is travelling in the $x$ direction. *P–SV* waves (i.e. $F_R$) have displacement in the $x$–$z$ directions and the *SH* waves ($F_L$) have displacement in the $y$ direction.

transversely isotropic material has five independent elastic tensor coefficients $C_{11}$, $C_{33}$, $C_{44}$, $C_{66}$ and $C_{13}$, which determine the velocities of different propagation angles $\theta$ as described in Thomsen (1986).

Routine substitution of the above in the full elastic wave equation (Aki & Richards 2009, eq. 2.74) gives us two decoupled systems of generalized quadratic eigenvalue problems (see Aki & Richards 2009, section 7.2 for working):

$$\omega^2 \left( \frac{C_{66}}{c^2} - \rho \right) l = \frac{\partial}{\partial z} \left( C_{44} \frac{\partial l}{\partial z} \right), \tag{2a}$$

$$k C_{13} \frac{\partial r_2}{\partial z} + k^2 (C_{11} - c^2 \rho) r_1 = \frac{\partial}{\partial z} \left( C_{44} \frac{\partial r_1}{\partial z} - k C_{44} r_2 \right), \tag{2b}$$

$$- k C_{44} \frac{\partial r_1}{\partial z} + k^2 (C_{44} - c^2 \rho) r_2 = \frac{\partial}{\partial z} \left( C_{33} \frac{\partial r_2}{\partial z} + k C_{13} r_1 \right), \tag{2c}$$

where (2b) and (2c) are coupled.

The solution to eq. (2a) yields the $F_L$ mode FZTW which is analogous to Love type surface waves and has particle motion only in the $y$ direction. The related eigenvalue is $\omega$ which corresponds to trapped frequencies for each particular phase speed ($c$) and the related eigenvector is the trapped mode $l(z)$. The solution to the coupled eqs (2b) and (2c) yields the $F_R$ type FZTWs which are analogous to Rayleigh type surface waves, and these have motion in the $x$ and $z$ directions. The eigenvalue in these two coupled equations is the wave number $k$ with eigenvectors $\{r_1(z), r_2(z)\}$. The lowest eigenvalue for each $c$ is called the fundamental and the higher eigenvalues are referred to as harmonics.

For $\omega$ to be real-valued in eq. (2a) and hence for the $F_L$ trapped mode to exist, we must have $c_{\min}^H = \min(\beta_x^H(z)) < c < \min(\beta_x^H(\pm\infty)) = c_{\max}^H$. For $F_R$ to exist, we must have $c_{\min}^V = \min(\beta_x^V(z)) < c < \min(\beta_x^V(\pm\infty)) = c_{\max}^V$. Note that the superscript H and V refer to *SH* and *SV* polarization respectively.

We use the anisotropy parameters that are defined by Thomsen (1986), these are:

$$\alpha_0 = \sqrt{\frac{C_{33}}{\rho}} = \alpha(0°), \tag{3a}$$

$$\beta_0 = \sqrt{\frac{C_{44}}{\rho}} = \beta^{\mathrm{V}}(90°) = \beta^{\mathrm{V}}(0°) = \beta^{\mathrm{H}}(0°), \tag{3b}$$

$$\epsilon = \frac{C_{11} - C_{33}}{2C_{33}} \Rightarrow \alpha(90°) = \alpha_0\sqrt{1 + 2\epsilon}, \tag{3c}$$

$$\gamma = \frac{C_{66} - C_{44}}{2C_{44}} \Rightarrow \beta^{\mathrm{H}}(90°) = \beta_0\sqrt{1 + 2\gamma}, \tag{3d}$$

$$\delta = \frac{(C_{13} + C_{44})^2 - (C_{33} - C_{44})^2}{2C_{33}(C_{33} - C_{44})}. \tag{3e}$$

For a fully isotropic media, we would have $\epsilon = \gamma = \delta = 0$. To visualize this parametrization of anisotropy, consider briefly the case of weak elastic anisotropy ($|\epsilon|, |\gamma|, |\delta| \ll 1$). In this case, it was shown in Thomsen (1986) that the velocities are approximately given by

$$\alpha(\theta) = \alpha_0\left[1 + \delta \sin^2(\theta)\cos^2(\theta) + \epsilon \sin^4(\theta)\right], \tag{4a}$$

$$\beta^{\mathrm{V}}(\theta) = \beta_0\left[1 + \frac{\alpha_0^2}{\beta_0^2}(\epsilon - \delta)\sin^2(\theta)\cos^2(\theta)\right], \tag{4b}$$

$$\beta^{\mathrm{H}}(\theta) = \beta_0\left[1 + \gamma \sin^2(\theta)\right]. \tag{4c}$$

### 2.3 Absorbing boundary conditions

We need to pose a boundary model on eqs (2). It is known that $l$, $r_1$, $r_2 \to 0$ as $z \to \pm\infty$ however significant computational improvements can be obtained by employing absorbing boundary conditions (Engquist & Majda 1977). To this end, we choose the computational domain to be bounded by $z_{\min}$ and $z_{\max}$. We approximate $C_{ij}$ and $\rho$ as constants in the regions outside the computational domain, that is, $z \le z_{\min}$ and $z \ge z_{\max}$. To compute the absorbing boundary condition we start with the analytic solutions to eqs (2) for the regions outside of the truncation boundaries. We then apply the conditions that $l$, $r_1$, $r_2 \to 0$ as $z \to \pm\infty$. This leaves us with the following equations:

$$l(z) = A_h \exp(\omega k_h z), \tag{5a}$$

$$r_1(z) = A_v S_1 \exp(\omega k_v z) + A_p P_1 \exp(\omega k_p z), \tag{5b}$$

$$r_2(z) = A_v S_2 \exp(\omega k_v z) + A_p P_2 \exp(\omega k_p z), \tag{5c}$$

where,

$$n = \begin{cases} -1, & \text{if } z = z_1, \\ 1, & \text{if } z = z_N, \end{cases} \tag{6a}$$

$$Q_0 = \left((2\epsilon + 1)c^{-2} - \alpha_0^{-2}\right)\left(c^{-2} - \beta_{0.}^{-2}\right), \tag{6b}$$

$$Q_1 = \alpha_0^{-2} + \beta_0^{-2} + 2c^{-2}\left((\alpha_0^2\beta_0^{-2} - 1)(\delta - \epsilon) - 1 - \epsilon\right), \tag{6c}$$

$$k_h = -n\sqrt{(2\gamma + 1)c^{-2} - \beta_0^{-2}}, \tag{6d}$$

$$k_v = -n\sqrt{\frac{1}{2}\left(-Q_1 - \sqrt{Q_1^2 - 4Q_0}\right)}, \tag{6e}$$

$$k_p = -n\sqrt{\frac{1}{2}\left(-Q_1 + \sqrt{Q_1^2 - 4Q_0}\right)}, \tag{6f}$$

$$S_1 = \left((2\epsilon + 1)\alpha_0^2 c^{-2} - 1 - k_v^2\beta_0^2\right)^{-1}, \tag{6g}$$

$$S_2 = \left(-k_v c^{-1}\sqrt{(\alpha_0^2 - \beta_0^2)\left((2\delta + 1)\alpha_0^2 - \beta_0^2\right)}\right)^{-1}, \tag{6h}$$

$$P_1 = \left((2\epsilon + 1)\alpha_0^2 c^{-2} - 1 - k_p^2\beta_0^2\right)^{-1}, \tag{6i}$$

$$P_2 = \left(-k_p c^{-1}\sqrt{(\alpha_0^2 - \beta_0^2)\left((2\delta + 1)\alpha_0^2 - \beta_0^2\right)}\right)^{-1}, \tag{6j}$$

and $A_h$, $A_v$, $A_p$ are arbitrary constants.

It can be shown that eqs (5) are the unique solution to the first order differential equations

$$\frac{\partial l}{\partial z} = \omega k_h l, \tag{7a}$$

$$\frac{\mathrm{d}r_1}{\mathrm{d}z} = k\xi[(S_1 P_2 k_v - P_1 S_2 k_p)r_1 + (k_p - k_v)S_1 P_1 r_2], \tag{7b}$$

$$\frac{\mathrm{d}r_2}{\mathrm{d}z} = k\xi[(k_v - k_p)S_2 P_2 r_1 + (S_1 P_2 k_p - P_1 S_2 k_v)r_2], \tag{7c}$$

where $\xi = c(S_1 P_2 - P_1 S_2)^{-1}$.

If eqs (7) are applied at the truncation boundaries then the interior solution will behave as though the solution domain goes to $\pm\infty$ and therefore eqs (7) are the absorbing boundary conditions.

### 2.4 Finite element approximation

We use the finite element method to solve eqs (2) with boundary conditions (7). In the finite element method, the solution is approximated by a weighted sum of $N$ basis functions. For example, we write $l(z) \approx \sum_{k=1}^N l(z_k)v_k(z)$, where the basis functions have the property that $v_k(z_k) = 1$ and $v_k(z_j) = 0$ for $k \ne j$, and where $z_k$, for $k = 1, 2, 3, \dots, N$ are a set of ordered locations (nodes) of the finite element mesh with $z_1 = z_{\min}$ and $z_N = z_{\max}$. Another property of the basis functions is that they are non-zero only on a region close to the corresponding nodes and in this non-zero region they can be represented as Lagrange interpolation polynomials of order $P$, which is referred to as the order of the approximation. Here, we choose the node locations specifically so that these polynomials have zeros at the so-called Lobatto points, leading to increased computational accuracy. For further details on the finite element scheme employed in this paper see Gulley (2017, section 1.4) or Pozrikidis (2005, chaps 1–2).

Let us define the vector **l** with entries $l_k = l(z_k)$ and the vectors **r₁** and **r₂** defined in the same way. We define the following elements of finite element matrices:

$$\mathbf{M}_{ji}^f = \int_{z_1}^{z_N} f(z)v_i(z)v_j(z)\mathrm{d}z, \tag{8a}$$

$$\mathbf{S}_{ji}^f = \int_{z_1}^{z_N} f(z)\frac{\partial v_i(z)}{\partial z}\frac{\partial v_j(z)}{\partial z}\mathrm{d}z, \tag{8b}$$

$$\mathbf{D}_{ji}^f = \int_{z_1}^{z_N} f(z) \frac{\partial v_i(z)}{\partial z} v_j(z) \mathrm{d}z, \tag{8c}$$

$$\mathbf{H}_{ji}^f = \int_{z_1}^{z_N} f(z) v_i(z) \frac{\partial v_j(z)}{\partial z} \mathrm{d}z, \tag{8d}$$

$$\mathbf{\Gamma}_{ji}^f = \begin{cases} -f(z_1)v_1(z_1)\frac{\mathrm{d}v_j}{\mathrm{d}z}|_{z_1}, & \text{if } i = j = 1, \\ f(z_N)v_N(z_N)\frac{\mathrm{d}v_j}{\mathrm{d}z}|_{z_N}, & \text{if } i = j = N, \\ 0, & \text{otherwise,} \end{cases} \tag{8e}$$

$$\mathbf{\Xi}_{ji}^f = \begin{cases} -f(z_1)v_1^2(z_1), & \text{if } i = j = 1, \\ f(z_N)v_N^2(z_N), & \text{if } i = j = N, \\ 0, & \text{otherwise,} \end{cases} \tag{8f}$$

where the subscripts refer to the $j$th row and $i$th column of the matrices and $f$ is a related function of $z$ which depends on which particular coefficient the matrix is related to. We compute the integrals using Gaussian quadrature.

Thus, following the standard finite element procedure, eqs (2) are approximated with the quadratic eigenvalue (matrix) problems

$$\mathbf{0} = (\mathbf{S}^{C44} - \mathbf{\Gamma}^{C44})\mathbf{l} - \omega^2(\mathbf{M}^\rho - c^{-2}\mathbf{M}^{C66})\mathbf{l}, \tag{9a}$$

$$\mathbf{0} = (\mathbf{S}^{C44} - \mathbf{\Gamma}^{C44})\mathbf{r}_1 + k(\mathbf{D}^{C13} - \mathbf{H}^{C44} + \mathbf{\Xi}^{C44})\mathbf{r}_2$$
$$+ k^2(\mathbf{M}^{C11} - c^2\mathbf{M}^\rho)\mathbf{r}_1, \tag{9b}$$

$$\mathbf{0} = (\mathbf{S}^{C33} - \mathbf{\Gamma}^{C33})\mathbf{r}_2 + k(\mathbf{H}^{C13} - \mathbf{\Xi}^{C13} - \mathbf{D}^{C44})\mathbf{r}_1$$
$$+ k^2(\mathbf{M}^{C44} - c^2\mathbf{M}^\rho)\mathbf{r}_2. \tag{9c}$$

Adopting the absorbing boundary model (eqs 7) causes the $\mathbf{\Gamma}$ matrices to be substituted by $\mathbf{\Xi}$ matrices. The finite element approximation, eqs (9), can now be written in the form

$$\mathbf{0} = \mathbf{S}^{C44}\mathbf{l} - \omega\mathbf{\Xi}^{g_0}\mathbf{l} - \omega^2(\mathbf{M}^\rho - c^{-2}\mathbf{M}^{C66})\mathbf{l}, \tag{10a}$$

$$\mathbf{0} = \mathbf{S}^{C44}\mathbf{r}_1 + k(\mathbf{D}^{C13} - \mathbf{H}^{C44} - \mathbf{\Xi}^{g_2-C44})\mathbf{r}_2,$$
$$- k\mathbf{\Xi}^{g_1}\mathbf{r}_1 + k^2(\mathbf{M}^{C11} - c^2\mathbf{M}^\rho)\mathbf{r}_1, \tag{10b}$$

$$\mathbf{0} = \mathbf{S}^{C33}\mathbf{r}_2 + k(\mathbf{H}^{C13} - \mathbf{\Xi}^{C13+g_3} - \mathbf{D}^{C44})\mathbf{r}_1,$$
$$- k\mathbf{\Xi}^{g_4}\mathbf{r}_2 + k^2(\mathbf{M}^{C44} - c^2\mathbf{M}^\rho)\mathbf{r}_2, \tag{10c}$$

where,

$$g_0(z_b) = C_{44}k_h, \tag{11a}$$

$$g_1(z_b) = C_{44}\xi(S_1 P_2 k_v - P_1 S_2 k_p), \tag{11b}$$

$$g_2(z_b) = C_{44}\xi(k_p - k_v)S_1 P_1, \tag{11c}$$

$$g_3(z_b) = C_{33}\xi(k_v - k_p)S_2 P_2, \tag{11d}$$

$$g_4(z_b) = C_{33}\xi(S_1 P_2 k_p - P_1 S_2 k_s). \tag{11e}$$

## 2.5 Derivation of the related linear eigenvalue equations

Next, we transform the generalized quadratic eigenvalue problems (eq. 10) to the generalized (non-quadratic, linear) eigenvalue problems. To this end, we define first the following (block) vector and matrices:

$$\mathbf{r} = \begin{bmatrix} \mathbf{r}_1 \\ \mathbf{r}_2 \end{bmatrix}, \tag{12a}$$

$$\mathbf{A}_S = \begin{bmatrix} \mathbf{S}^{C44} & \mathbf{0} \\ \mathbf{0} & \mathbf{S}^{C33} \end{bmatrix}, \tag{12b}$$

$$\mathbf{A}_D = \begin{bmatrix} \mathbf{0} & \mathbf{D}^{C13} - \mathbf{H}^{C44} \\ \mathbf{H}^{C13} - \mathbf{D}^{C44} & \mathbf{0} \end{bmatrix}, \tag{12c}$$

$$\mathbf{A}_F = \begin{bmatrix} \mathbf{M}^{C11} & \mathbf{0} \\ \mathbf{0} & \mathbf{M}^{C44} \end{bmatrix}, \tag{12d}$$

$$\mathbf{A}_M = \begin{bmatrix} \mathbf{M}^\rho & \mathbf{0} \\ \mathbf{0} & \mathbf{M}^\rho \end{bmatrix}, \tag{12e}$$

$$\mathbf{A}_\Xi = \begin{bmatrix} \mathbf{\Xi}^{g_1} & \mathbf{\Xi}^{g_2-C44} \\ \mathbf{\Xi}^{g_3+C13} & \mathbf{\Xi}^{g_4} \end{bmatrix}, \tag{12f}$$

where $\mathbf{0}$ is a zero matrix of appropriate dimensions. The eqs (10) can now be written as

$$\mathbf{0} = [\mathbf{S}^{C44} - \omega\mathbf{\Xi}^{g_0} - \omega^2(\mathbf{M}^\rho - c^{-2}\mathbf{M}^{C66})]\mathbf{l}, \tag{13a}$$

$$\mathbf{0} = [\mathbf{A}_S + k(\mathbf{A}_D - \mathbf{A}_\Xi) + k^2(\mathbf{A}_F - c^2\mathbf{A}_M)]\mathbf{r}. \tag{13b}$$

The eqs (13) specify two uncoupled quadratic eigenvalue problems. To reduce these to generalized (linear, non-quadratic) eigenvalue problems, we define further:

$$\mathbf{l}^* = \begin{bmatrix} \mathbf{l} \\ \omega\mathbf{l} \end{bmatrix}, \tag{14a}$$

$$\mathbf{r}^* = \begin{bmatrix} \mathbf{r} \\ k\mathbf{r} \end{bmatrix}, \tag{14b}$$

$$\widetilde{\mathbf{S}}^L = \begin{bmatrix} \mathbf{0} & \mathbf{I} \\ \mathbf{S}^{C44} & -\mathbf{\Xi}^{g_0} \end{bmatrix}, \tag{14c}$$

$$\widetilde{\mathbf{M}}^L = \begin{bmatrix} \mathbf{I} & \mathbf{0} \\ \mathbf{0} & \mathbf{M}^\rho - c^{-2}\mathbf{M}^{C66} \end{bmatrix}, \tag{14d}$$

$$\widetilde{\mathbf{S}}^R = \begin{bmatrix} \mathbf{0} & \mathbf{I} \\ -\mathbf{A}_S & \mathbf{A}_\Xi - \mathbf{A}_D \end{bmatrix}, \tag{14e}$$

$$\widetilde{\mathbf{M}}^R = \begin{bmatrix} \mathbf{I} & \mathbf{0} \\ \mathbf{0} & \mathbf{A}_F - c^2 \mathbf{A}_M \end{bmatrix}, \tag{14f}$$

where $\mathbf{I}$ are identity matrices of appropriate dimensions. Thus, the eqs (13) can be written in the form of

$$\widetilde{\mathbf{S}}^L \mathbf{l}^* = \omega \widetilde{\mathbf{M}}^L \mathbf{l}^*, \tag{15a}$$

$$\widetilde{\mathbf{S}}^R \mathbf{r}^* = k \widetilde{\mathbf{M}}^R \mathbf{r}^*. \tag{15b}$$

We note that the above representation is not unique. There are also representations in which the matrices $\widetilde{\mathbf{S}}, \widetilde{\mathbf{M}}$ are symmetric which would yield certain computational advantages. In our case, the choice we have made yield diagonally dominant matrices, which we exploit in the mass lumping below.

## 2.6 Mass lumping

The eqs (15) define generalized eigenvalue problems. In the chosen form, the matrices on the right-hand side ($\widetilde{\mathbf{M}}$) are made up of matrices on the diagonal blocks which are either identity matrices or of the mass matrix type $\mathbf{M}^f$. For these, we employ mass lumping (Cohen *et al.* 1993) in which the matrices $\widetilde{\mathbf{M}}$ are approximated by diagonal matrices $\widehat{\mathbf{M}}$ as follows:

$$\widehat{\mathbf{M}}_{ji} = \begin{cases} \sum_{i=1}^{N} \widetilde{\mathbf{M}}_{ji}, & \text{if } i = j, \\ 0, & \text{if } i \neq j. \end{cases} \tag{16}$$

Mass lumping is equivalent to calculating the $\mathbf{M}^f_{ji}$ integrals in eqs (8) using inexact quadrature. Let $P$ be the polynomial order of the basis functions used, then the integrands of the $\mathbf{M}^f_{ji}$ integrals are at least of order $2P$ (equality when $f = $ constant). The mass lumping approximation is equivalent to evaluating these integrals with Lobatto quadrature that is exact when the integrands have polynomial order up to $2P - 1$ (chap. 3, Pozrikidis 2005). As $2P - 1 < 2P$, mass lumping is always an approximation but it is often a feasible one.

Since the approximate $\widehat{\mathbf{M}}$ is diagonal, we define $\widehat{\mathbf{S}} = \widehat{\mathbf{M}}^{-1} \widetilde{\mathbf{S}}$ to reduce the eqs (15) to the ordinary eigenvalue problems

$$\widehat{\mathbf{S}}^L(c) \mathbf{l}^* = \omega \mathbf{l}^*, \tag{17a}$$

$$\widehat{\mathbf{S}}^R(c) \mathbf{r}^* = k \mathbf{r}^*, \tag{17b}$$

where we have indicated $c$ to stress that these matrices depend on the phase speed. The eigenvalues of the problems (17) can be solved with various methods such as the pre-built eigenvalue solvers in MATLAB® (chap. 7, Golub & Loan 2013) which we use here. An example of a velocity model and eigenvectors ($l(z), r_1(z), r_2(z)$) from three different eigenvalues (trapped frequencies) are shown in Fig. 3.

### 2.6.1 Reducing errors induced by mass lumping

The use of mass lumping allows us to solve the much less computationally intensive simple eigenvalue matrix problem. Numerical evaluation of the mass lumping approximation indicates that the loss of accuracy associated with the mass lumping is small but tends to increase at higher frequencies ($\omega$) and elastic models with high gradients within an element. In the following, we make use of a correction that can be applied to improve the eigenvalue estimates.
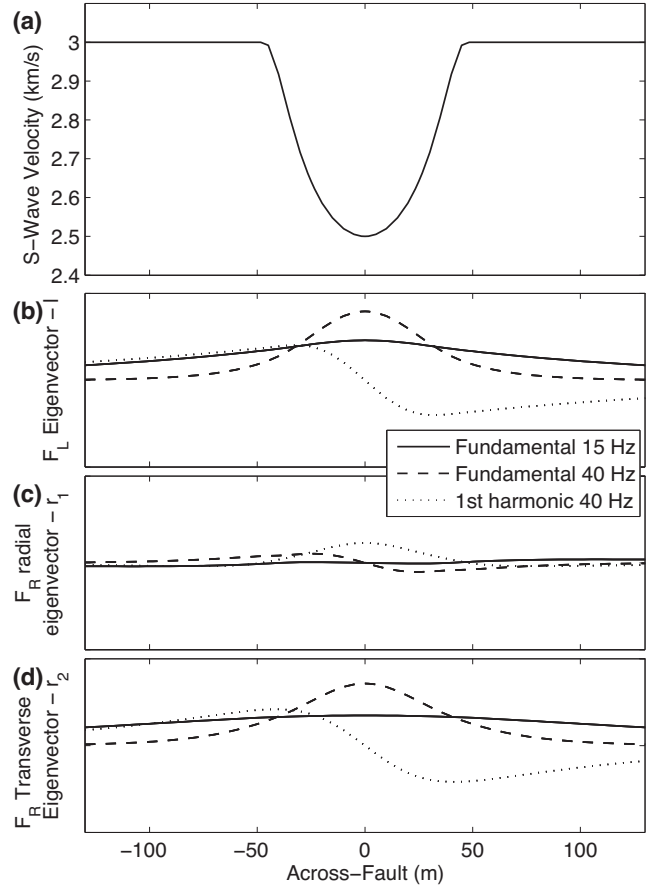


**Figure 3.** Trapped modes of a velocity model. (a) *S*-wave velocity model used. The *P*-wave velocity and the density have a similar shape to the *S*-wave velocity but with ranges of 5–5.3 km s$^{-1}$ and 2.6–2.7 g cm$^{-3}$, respectively. There is no anisotropy assumed here. (b–d) Examples of the eigenvectors (trapped modes) for three different eigenvalues (frequencies). The eigenvectors are normalized by kinetic energy.

Multiplying eqs (2) by $l$, $r_1$ and $r_2$, respectively, and carrying out integration by parts before summing the $F_R$ equations (see Aki & Richards 2009, section 7.3 for details), yields the following equations:

$$0 = \omega^2 \left( c^{-2} I_2^l - I_1^l \right) + I_3^l, \tag{18a}$$

$$0 = k^2 (I_2^r - c^2 I_1^r) + k I_3^r + I_4^r, \tag{18b}$$

where the $I_k^{r,l}$ are the energy integrals,

$$I_1^l = \frac{1}{2} \int_{-\infty}^{\infty} \rho l^2 \, dz, \tag{19a}$$

$$I_2^l = \frac{1}{2} \int_{-\infty}^{\infty} C_{66} l^2 \, dz, \tag{19b}$$

$$I_3^l = \frac{1}{2} \int_{-\infty}^{\infty} C_{44} \left( \frac{dl}{dz} \right)^2 \, dz, \tag{19c}$$

$$I_1^r = \frac{1}{2} \int_{-\infty}^{\infty} \rho \left( r_1^2 + r_2^2 \right) \, dz, \tag{19d}$$

$$I_2^r = \frac{1}{2}\int_{-\infty}^{\infty} C_{11}r_1^2 + C_{44}r_2^2 \, \mathrm{d}z, \tag{19e}$$

$$I_3^r = \int_{-\infty}^{\infty} C_{13}r_1 \frac{\mathrm{d}r_2}{\mathrm{d}z} - C_{44}r_2 \frac{\mathrm{d}r_1}{\mathrm{d}z} \, \mathrm{d}z, \tag{19f}$$

$$I_4^r = \frac{1}{2}\int_{-\infty}^{\infty} C_{33}\left(\frac{\mathrm{d}r_2}{\mathrm{d}z}\right)^2 + C_{44}\left(\frac{\mathrm{d}r_1}{\mathrm{d}z}\right)^2 \, \mathrm{d}z. \tag{19g}$$

The above equations are given in Aki & Richards (2009, section 7.3) for isotropic surface waves, but they are presented here for transversely isotropic trapped waves. These integrals are computed from $-\infty$ to $+\infty$. To compute these integrals we must account for the fact that we have only computed the eigenvectors between $z_{\min} = z_1$ and $z_{\max} = z_N$ and the energy that is absorbed by the absorbing boundaries. To do this we make use of the fact that we already know the form of the wave outside of the boundaries, these are given in eq. (5). The computational procedure is defined in the following derivation:

$$
\begin{aligned}
I_1^l &= \frac{1}{2}\int_{-\infty}^{\infty} \rho l^2 \mathrm{d}z, \\
&= \frac{1}{2}\int_{-\infty}^{z_1} \rho l^2 \mathrm{d}z + \frac{1}{2}\int_{z_1}^{z_N} \rho l^2 \mathrm{d}z + \frac{1}{2}\int_{z_N}^{\infty} \rho l^2 \mathrm{d}z, \\
&= \frac{\rho(z_1)}{2\omega k_h(z_1)}l^2(z_1) + \frac{1}{2}\mathbf{l}^\top \mathbf{M}^\rho \mathbf{l} - \frac{\rho(z_N)}{2\omega k_h(z_N)}l^2(z_N), \\
&= \frac{1}{2}\mathbf{l}^\top \mathbf{M}^\rho \mathbf{l} + \sum_{\pm} \frac{-n\rho}{2\omega k_h}l^2,
\end{aligned}
\tag{20a}
$$

$$I_2^l = \frac{1}{2}\mathbf{l}^\top \mathbf{M}^{C_{66}}\mathbf{l} + \sum_{\pm} \frac{-nC_{66}}{2\omega k_h}l^2, \tag{20b}$$

$$I_3^l = \frac{1}{2}\mathbf{l}^\top \mathbf{S}^{C_{44}}\mathbf{l} + \sum_{\pm} \frac{-nC_{44}\omega k_h}{2}l^2, \tag{20c}$$

$$I_1^r = \frac{1}{2}\mathbf{r}^\top \mathbf{A}_M \mathbf{r} + \sum_{\pm} \hat{\mathbf{r}}^\top (\rho \mathbb{I}_{r1} + \rho \mathbb{I}_{r2})\hat{\mathbf{r}}, \tag{20d}$$

$$I_2^r = \frac{1}{2}\mathbf{r}^\top \mathbf{A}_F \mathbf{r} + \sum_{\pm} \hat{\mathbf{r}}^\top (C_{11}\mathbb{I}_{r1} + C_{44}\mathbb{I}_{r2})\hat{\mathbf{r}}, \tag{20e}$$

$$I_3^r = \mathbf{r}_2^\top \mathbf{H}^\lambda \mathbf{r}_1 - \mathbf{r}_1^\top \mathbf{H}^\mu \mathbf{r}_2 + \sum_{\pm} \hat{\mathbf{r}}^\top \mathbb{I}_3 \hat{\mathbf{r}}, \tag{20f}$$

$$I_4^r = \frac{1}{2}\mathbf{r}^\top \mathbf{A}_S \mathbf{r} + \sum_{\pm} \hat{\mathbf{r}}^\top (C_{44}\mathbb{I}_{dr1} + C_{33}\mathbb{I}_{dr2})\hat{\mathbf{r}}, \tag{20g}$$

where we have shown the derivation only for $I_1^l$ and $\sum_{\pm} f(z) = f(z_1) + f(z_N)$ and $(\cdot)^\top$ denotes transpose. We have also used the following matrices:

$$\hat{\mathbf{r}} = \frac{\xi}{c}\begin{bmatrix} P_2 & -P_1 \\ -S_2 & S_1 \end{bmatrix}\begin{bmatrix} r_1 \\ r_2 \end{bmatrix}, \tag{21a}$$

$$\mathbb{I}_{r1} = \frac{-n}{2\omega}\begin{bmatrix} S_1 & 0 \\ 0 & P_1 \end{bmatrix}\begin{bmatrix} \frac{1}{k_v} & \frac{2}{k_v+k_p} \\ \frac{2}{k_v+k_p} & \frac{1}{k_p} \end{bmatrix}\begin{bmatrix} S_1 & 0 \\ 0 & P_1 \end{bmatrix}, \tag{21b}$$

$$\mathbb{I}_{r2} = \frac{-n}{2\omega}\begin{bmatrix} S_2 & 0 \\ 0 & P_2 \end{bmatrix}\begin{bmatrix} \frac{1}{k_v} & \frac{2}{k_v+k_p} \\ \frac{2}{k_v+k_p} & \frac{1}{k_p} \end{bmatrix}\begin{bmatrix} S_2 & 0 \\ 0 & P_2 \end{bmatrix}, \tag{21c}$$

$$\mathbb{I}_{dr1} = \frac{-n\omega}{2}\begin{bmatrix} S_1 & 0 \\ 0 & P_1 \end{bmatrix}\begin{bmatrix} k_v & \frac{2k_v k_p}{k_v+k_p} \\ \frac{2k_v k_p}{k_v+k_p} & k_p \end{bmatrix}\begin{bmatrix} S_1 & 0 \\ 0 & P_1 \end{bmatrix} \tag{21d}$$

$$\mathbb{I}_{dr2} = \frac{-n\omega}{2}\begin{bmatrix} S_2 & 0 \\ 0 & P_2 \end{bmatrix}\begin{bmatrix} k_v & \frac{2k_v k_p}{k_v+k_p} \\ \frac{2k_v k_p}{k_v+k_p} & k_p \end{bmatrix}\begin{bmatrix} S_2 & 0 \\ 0 & P_2 \end{bmatrix}, \tag{21e}$$

$$\mathbb{I}_3 = \frac{n}{2}\begin{bmatrix} (C_{44}-C_{13})S_1 S_2 & g \\ g & (C_{44}-C_{13})P_1 P_2 \end{bmatrix}, \tag{21f}$$

where

$$g = \frac{C_{44}(S_1 P_2 k_v + S_2 P_1 k_p) - C_{13}(S_1 P_2 k_p + S_2 P_1 k_s)}{k_v + k_p}. \tag{21g}$$

As has been mentioned previously, an initial estimate for the eigenvectors and eigenvalues can be obtained from the mass lumped eqs (17). We can then use these estimates to compute the energy ($I$) using eqs (20). Once this has been done we can re-estimate the eigenvalues using eqs (18). It has been shown in Aki & Richards (2009, section 7.3) that estimating $\omega$ using eq. (18a) is accurate even if there are first order errors in the eigenvectors and eigenvalues used to compute the energy integrals. While there is no such proof shown for eq. (18b) we note the similarity between eqs (18) and the eigenvalue perturbation method (Golub & Loan 2013), which is used to update eigenvalues when small changes are made to matrices (in our case this small change is mass lumping). Our numerical experiments show that this correction causes a significant reduction in error, and that this reduction is greater than that obtained using eigenvalue perturbation methods. An example of the relative errors of the mass lumped solution with and without the correction are shown in Fig. 4. We assess that the errors induced by the mass lumping with the correction are small enough to be dominated by the overall approximate character of the velocity model. Numerical experiments suggest that using mass lumping together with the correction is up to 50 per cent faster than using the un-lumped equations however precise computational speeds and speed ups are determined by the polynomial order and number of elements used.

## 2.7 Computation of group velocities

The solution of (18) can then be used to find the frequency $\omega$ as a function of phase speed $c$ where $k = \omega/c$ for the $F_L$ and $F_R$ modes. In Aki & Richards (2009, chap. 7), it was shown that the group velocities $U^l$ and $U^r$ for $F_L$ and $F_R$, respectively, are given by

$$U^l(k, \omega) = \frac{I_2^l}{cI_1^l}, \tag{22a}$$

$$U^r(k, \omega) = \frac{I_2^r + \frac{I_3^r}{2k}}{cI_1^r}. \tag{22b}$$

With the above, we can compute $U$ and $\omega$ for any $c$. We want, however, to compute $U$ as a function of $\omega$. In order to explain our approach and to justify our choice of method, we will start by briefly discounting two standard approaches. The first standard way to compute $U$ as a function of $\omega$ would be to iteratively (using the
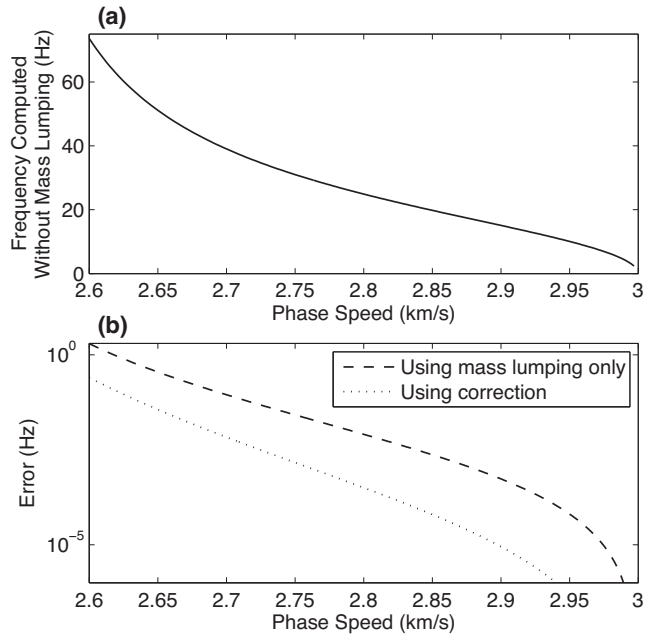
**Figure 4.** The effect of proposed mass lumping and correction. (a) The frequencies (eigenvalues) of the $F_L$ fundamental harmonic computed without using mass lumping (i.e. eq. 15). The velocity model can be seen in Fig. 3(a). Two sixth-order basis functions are used for this computation. (b) The errors induced by computing the eigenvalues using mass lumping and using the mass lumping correction. It can be seen that the errors of using mass lumping are small but the mass lumping correction reduces these errors by an order of magnitude.

Gauss-Newton method, for example) find the $c$ corresponding to a desired $\omega$ and subsequently compute the group velocity $U$. This would, however, be computationally expensive, since this procedure would need to be carried out for all required $\omega$ and each $\omega$ would require many eigenvalue computations in the iterative process. The second standard method would be to use a spline interpolation between a set of pre-computed $\{U, \omega\}$ points. For a linear spline to be sufficiently accurate, we would require many points to be pre-computed, which would be computationally expensive. To improve on this, we could use a quadratic spline; however, due to the unavoidably irregular spacing between known $\omega$ points, a quadratic spline that uses three points suffers heavily from Runge's phenomenon and is inaccurate as pointed out by Pozrikidis (2005).

Our method for computing $U$ as a function of $\omega$ uses a quadratic spline that has even $\omega$ point spacing over one quadratic interpolation and so does not suffer from Runge's phenomenon. To derive our method, we start from the definition of group velocity $U = \frac{d\omega}{dk}$. Assuming that $M$ pre-computed pairs of $\{U, \omega\}$ are ordered, we can consider the $j$th value ($j < M$) and we can write

$$U = \frac{d\omega}{dk} \Rightarrow k_{j+1} - k_j = \int_{\omega_j}^{\omega_{j+1}} \frac{d\omega}{U(\omega)}. \tag{23}$$

Provided $M$ is large enough (e.g. $M \sim 20$ with evenly spaced c values), the Simpson's rule will be accurate enough to compute the above integral, thus

$$k_{j+1} - k_j = \int_{\omega_j}^{\omega_{j+1}} \frac{d\omega}{U(\omega)}, \tag{24a}$$

$$\approx \frac{\omega_{j+1} - \omega_j}{6} \left( \frac{1}{U_j} + \frac{4}{U_{j+\frac{1}{2}}} + \frac{1}{U_{j+1}} \right), \tag{24b}$$
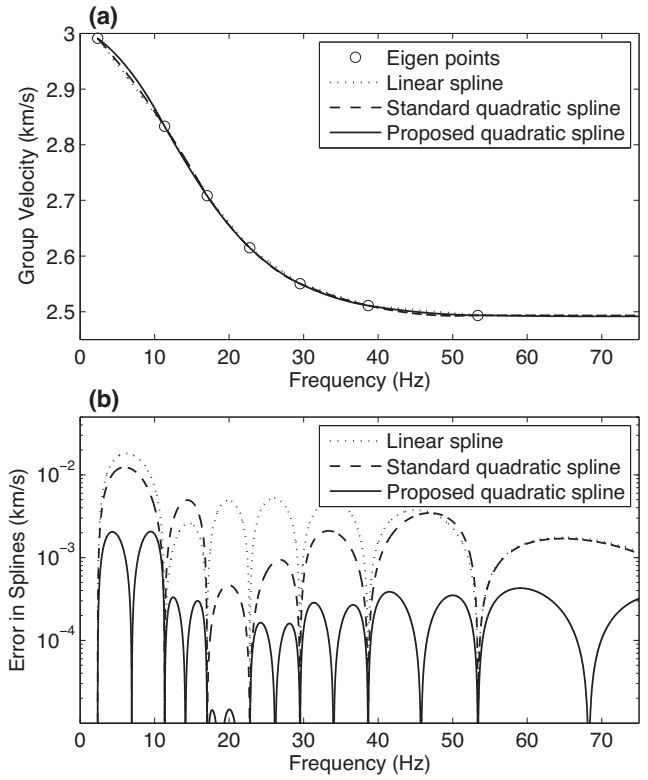


**Figure 5.** The effect of proposed group velocity interpolation methodology. (a) The $F_L$ fundamental dispersion curve for the velocity model seen in Fig. 3(a). The circles are the computed eigenvalues and corresponding group velocities and the lines show the different interpolation methods between these known points. (b) The errors induced by the different interpolation methods. It can be seen that the errors using the quadratic spline developed in this paper are around an order of magnitude more accurate.

where $U_{j+\frac{1}{2}} = U(\frac{\omega_{j+1}+\omega_j}{2})$. Rearranging leaves us with

$$U_{j+\frac{1}{2}} \approx 4 \left( 6 \frac{k_{j+1} - k_j}{\omega_{j+1} - \omega_j} - \frac{1}{U_j} - \frac{1}{U_{j+1}} \right)^{-1}. \tag{25}$$

This gives us an extra point in the middle of $\omega_j$ and $\omega_{j+1}$ that can be used for the quadratic spline between these two points. The accuracy of this method is shown in Fig. 5. We can now find $U$ for any $\omega$ by only pre computing $M \sim 20$ eigenvalues. Thus, we now have an efficient way of computing the dispersion curves for any arbitrary transversely isotropic velocity model.

## 2.8 Calculation of FZTW waveforms

Green's (amplitude) function representations can be used to compute the FZTW waveform induced by different source types, including a moment tensor point source, as seen in Aki & Richards (2009, sections 7.4 and 7.5). These representations are based both on the trapped modes (eigenvectors) and the associated resonant frequencies (eigenvalues) which can be computed using the approach described above. Previously, $F_L$ have been computed by Li & Leary (1990) and Li *et al.* (2012) using this approach.

The Green's representation for the waveform (three components of the displacement) $s$ from a single type of guided wave is of the

form

$$s(r, \phi, z, t) = \sum_{H=1}^{\infty} \int_{\omega_H^*}^{\infty} g(\omega_H, k_H, r, \phi, z) \exp\left(i(k_H(\omega)r - \omega_H t)\right) d\omega \tag{26}$$

where $r$ is the distance from the source to the receiver along-fault, $z$ is the distance from the centre of the fault, $\phi$ is the angle on the $x$-$y$ plane, and $t$ is time. The waveform $s$ is the (vector-valued) displacement in the three directions and $g$ is the (vector-valued) Green's function. The Green's function $g$ depends on the type and properties of the source, the elastic model and the (possible) attenuation. The index $H$ is the harmonic number, and typically only the first few harmonics are needed since the higher harmonics are strongly attenuated or are not generated in the first place. Furthermore, each harmonic has a minimum frequency $\omega_H^* = \omega_H(c_{\max})$.

For the computation of the integrals in eq. (26) by any quadrature scheme, we need to compute the values $g(\omega_H, k_H, r, \phi, z)$ at the quadrature points (frequencies). To compute each of these, we need to solve the respective eigenvalue problems, which is computationally the most complex task. To minimize the number of solutions to eigenvalue problems, we aim first to change the integration with respect to $\omega$ into an integral with respect to the phase speed $c$. Let us define the following functions:

$$\frac{d\omega_H}{dc} = \left(\frac{dc}{d\omega_H}\right)^{-1} = \left(\frac{d(\omega_H/k_H)}{d\omega_H}\right)^{-1} = \frac{k_H^2}{k_H - \omega_H/U_H}, \tag{27a}$$

$$\frac{dk_H}{dc} = \left(\frac{dc}{dk_H}\right)^{-1} = \left(\frac{d(\omega_H/k_H)}{dk_H}\right)^{-1} = \frac{k_H^2}{k_H U_H - \omega_H}, \tag{27b}$$

$$\hat{g}_H(c, r, \phi, z) = -g(\omega_H, k_H, r, \phi, z)\frac{d\omega_H}{dc}, \tag{27c}$$

$$\phi_H(c, x, t) = k_H(c)r - \omega_H(c)t, \tag{27d}$$

where $U_H = d\omega_H/dk_H$ is the group velocity calculated from the eqs (22). As a result changing the integration variable, the definite integrals are now over a finite interval,

$$s(r, \phi, z, t) = \sum_{H=1}^{\infty} \int_{c_{\min}}^{c_{\max}} \hat{g}_H(c, r, \phi, z) \exp\left(i\phi_H(c, x, t)\right) dc, \tag{28}$$

where $c_{\min}$ and $c_{\max}$ are the corresponding integration limits over $c$. For the quadrature with respect to $c$, we can choose the quadrature points to be evenly spaced. The negative sign in eq. (27c) is due to having $\omega_H(c_{\max}) = \omega_H^*$ and $\omega_H(c_{\min}) = \infty$ and the related exchange of integration limits.

To interpolate between values of $\omega$ and $k$ we utilize the fact that $\frac{d\omega}{dc}$ and $\frac{d\omega}{dk}$ are known at each point (eqs 27a–27b). This allows us to interpolate between the known $k$ and $\omega$ points with the third order polynomial spline that has the correct derivative and correct value at each known point. This cubic interpolation loses accuracy near $c_{\min}$ and $c_{\max}$ because the magnitude of $\frac{d\omega}{dc}$ or $\frac{dk}{dc}$ tends to $\infty$ near these boundaries. In practice, this is not an issue since $\hat{g} \approx 0$ near $c_{\min}$ and $c_{\max}$. Once we have increased the number of known points using this cubic spline we can then numerically integrate by treating $\hat{g}, k, \omega$ as linear functions between known points (e.g. Aki & Richards 2009).

An example of a computed waveform generated by an infinite line source using this interpolation method is shown in Fig. 6. It can be seen that using this interpolation method reduces the error by around an order of magnitude.
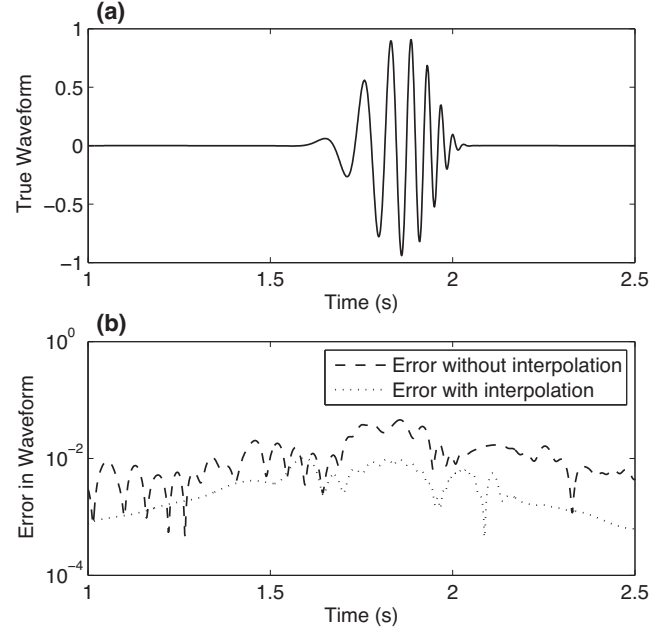


**Figure 6.** Effect of interpolating extra frequency and wavenumber points before the Green's functions are integrated to produce a waveform. (a) True $F_L$ waveform (displacement amplitude) for an infinite line source (2-D) using the velocity profile shown in Fig. 3(a). The source and receiver are centred in the fault zone and only the fundamental harmonic is shown. This 'true' waveform is computed using 10 000 eigenvalues. (b) The error in the waveform when it is calculated using 20 eigenvalues only and when an additional 20 points are interpolated between each eigenvalue and amplitude point. It can be seen that using the interpolation method increases accuracy by around an order of magnitude.

## 3 COMPARISON WITH 2-D FULL WAVEFORM SIMULATION

In order to investigate the advantages and disadvantages of the proposed method of computing FZTW waveforms, we compare it with a 2-D SH full waveform finite element method (Gulley 2017, chaps 1–2). This 2-D simulator was used because it allows the use of the 2-D equivalent of the 1-D elements used in this paper and so the simulations can be made that have similar spatial accuracy. In addition to this, the methods proposed in this paper and the 2-D method from Gulley (2017) are both written in MATLAB® and so speed comparisons are more relevant. This 2-D finite element method is comparable to the well-established method SPECFEM2D (Komatitsch & Tromp 1999). The velocity model used in the simulations can be seen in Fig. 1 (100 m wide) and the source is a 10 Hz Ricker-wavelet located 4 km from the receiver in the centre of the fault zone. The comparison between the method proposed in this paper and the 2-D full waveform method can be seen in Fig. 7.

The 2-D finite element method used a finite element mesh with 4th order elements that are isosceles right-angle triangles with the equal edges being 50 m long while the method proposed in this paper uses two 50 m wide fourth-order elements. The computational domain of the 2-D finite element method is 1.6 km wide by 6.5 km long and angled 1st order paraxial absorbing boundary conditions are used (Gulley 2017, chap. 2). Time stepping is done using the 2nd order method of Newmark (1959) with a time step of $10^{-3}$ s.

It can be seen in Fig. 7 that the method of computing FZTW waveforms proposed in this paper and the 2-D full waveform finite element method produce similar waveforms: they have a correlation of 99 per cent (normalized cross-correlation). While the differences
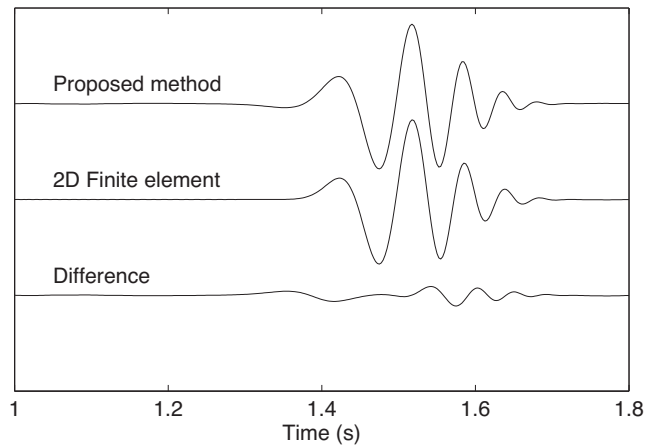
**Figure 7.** Comparison between 2-D $F_L$ waveforms produced by the method proposed in this paper and a 2-D time domain finite element method (Gulley 2017, chaps 1–2). The velocity model is the same as in Fig. 1 (100 m wide waveguide) and the point source is a 10 Hz Ricker-wavelet located 4 km from the receiver. The bottom waveform is the 2-D finite element waveform less the waveform from the proposed method.

are small they can be attributed to a number of causes. At the start of the waveforms (1.3–1.45 s) there is a small difference in the two low frequency signals. This is an error in the 2-D full waveform simulation which is due to the low frequency trapped modes being wider than the 1.6 km wide computational domain used (see Fig. 3). A wider computational domain would be needed to sufficiently trap these low frequencies. Towards the end of the simulated waveforms (1.5–1.65 s) the difference increases in amplitude, the likely causes of this being numerical dispersion of the Newmark's time stepping method (Noh *et al.* 2013) and superfluous reflections of the absorbing boundaries. These can be improved through different time stepping methods (see Noh *et al.* 2013) or improved absorbing boundary techniques (e.g. Komatitsch & Tromp 2003). Also of note is that the 2-D full waveform simulation does not display a direct body *S*-wave. This is what is expected with this idealized 1-D velocity model as all energy travelling towards the receiver is travelling at an angle such that it will critically reflect off the fault zone walls and is therefore part of the FZTW. Although not shown in this manuscript, there is body *S*-wave energy travelling at more perpendicular angles away from the fault zone in the 2-D full waveform simulation.

The time to compute the waveform on a single core using the method shown in this paper is on the order of $10^{-1}$ s, whereas the time to compute the 2-D full waveform simulation is on the order of $10^2$ s. In addition to this, the time to compute the full waveform will significantly increase if the source is further away from the receiver or the 3-D waveform is of interest. This clearly shows that the method proposed in this paper is significantly faster, even if more efficient full waveform solvers with parallel computation are used. The method proposed in this paper is, however, only useful for computing the full FZTW waveforms when the velocity model of interest lends itself to a 1-D approximation. More complex velocity models still require full waveform solvers.

## 4 COMPARISON WITH LAYERED VELOCITY MODEL

The strength of this finite element method is its ability to deal with gradational velocity models efficiently. Gradational velocity
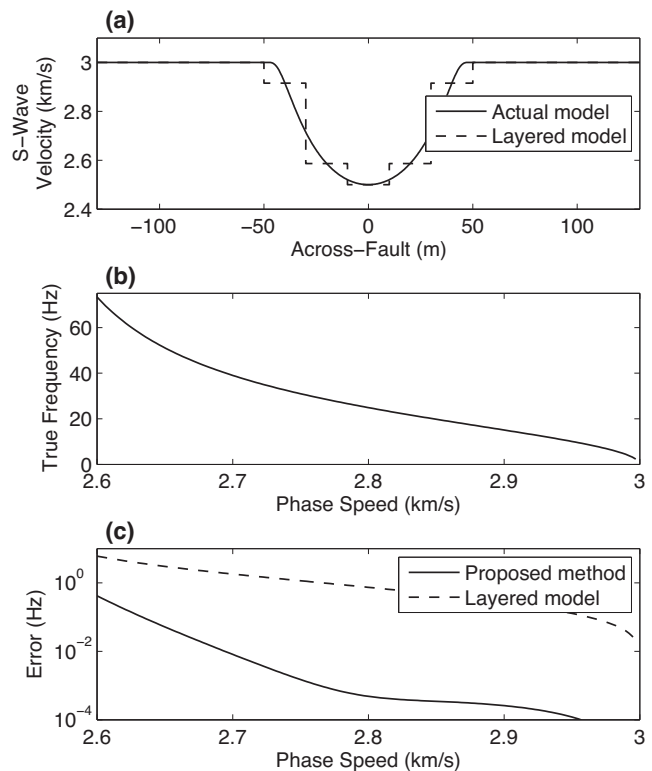


**Figure 8.** Shows the effectiveness of the proposed finite element method of dealing with gradational velocity models. (a) The true velocity model and a seven layer approximation. (b) The true eigenvalues (frequencies) of the $F_L$ fundamental harmonic for the true velocity model that is calculated using 50 seventh-order basis functions. (c) The errors induced by using one sixth-order polynomial (7 unknowns) as a finite element basis or using a seven homogeneous layer approximation. It can be seen that the finite element method is several orders of magnitude more accurate.

may also be approximated using many homogenous layers. This allows one to use methods such as the propagator matrix (Thomson 1950; Haskell 1953). To compare these two methods, we compute the eigenvectors with one seven point polynomial basis vector and compare the result to the solution from a seven layer approximation of the velocity model. Such a model is shown in Fig. 8. These two methods both have the same number of unknowns and therefore similar computational complexity and computational time. Fig. 8 shows that the finite element method used here is significantly more accurate when dealing with gradational velocity models. Further computations suggest that, typically, ~40 homogenous layers are needed to approximate the velocity model seen in Fig. 8 in order to obtain accuracy similar to that derived from the finite element method with one seven point polynomial basis function.

If the velocity model of interest can be well approximated by a small number of homogenous layers, then it is likely that the methods in this paper are less efficient than other methods (e.g. Thomson 1950; Haskell 1953; Li & Leary 1990; Ben-Zion 1998; Li *et al.* 2012). Lithologically bounded waveguides such as coal seams can often be thought of as homogenous layers, and while the methodology in this paper will work in these situations, previously published methods are more efficient. Many fault zones, however, can be thought of as having gradational boundaries (Leary *et al.* 1987), therefore our methodology is primarily aimed at FZTWs.

## 5 DISCUSSION

We proposed a computational scheme to compute the dispersion curves and observed waveforms corresponding to arbitrary transversely isotropic velocity models. The motivation for a computationally efficient approach is to allow the use of such a model in inversions. While the forward model may need to be computed a large number of times when employing, for example, a Gauss-Newton type algorithm, we note that the exploration of the (posterior) uncertainty using a Markov chain Monte Carlo algorithm typically calls for forward computations in the order of millions of times. In such cases, even moderate speed-ups are welcome.

The main limitation of this model is that it assumes no variation in structure in the direction of FZTW propagation. While this model is an improvement on previously employed semi-analytic models, even this model is unrealistic since the elastic properties of the fault-zone and country-rock typically change with depth due to increasing pressures and temperatures. To try to reduce the above limitation, an approximation can be made that represents this 2-D variability with 1-D slices, as was done in Wu *et al.* (2010). However, in general, a fault zone that changes in width will have different dispersion and amplitude information due to different reflection angles than a model that is based on 1-D slices (Li & Vidale 1996). Such a model also does not allow for variation in the third (transverse to propagation) direction.

We have assumed that transverse-isotropy is the dominant form of anisotropy. It is possible, however, that the anisotropic structure of fault zones is more general (Li *et al.* 1987). The proposed approach could in principle be generalized to an arbitrary anisotropic model. This would, however, incur a significant additional numerical cost since the displacements in all three directions would be coupled where currently the *SH* motion is decoupled.

## ACKNOWLEDGEMENTS

## REFERENCES

Aki, K. & Richards, P.G., 2009. *Quantitative Seismology,* 2nd edn, University Science Books.

Ben-Zion, Y., 1998. Properties of seismic fault zone waves and their utility for imaging low-velocity structures, *J. geophys. Res.,* **103,** 12 567–12 585.

Ben-Zion, Y., Katz, S. & Leary, P., 1992. Joint inversion of fault zone head waves and direct P arrivals for crustal structure near major faults, *J. geophys. Res.,* **97**(B2), 1943–1951.

Ben-Zion, Y. *et al.*, 2003. A shallow fault-zone structure illuminated by trapped waves in the Karadere–Duzce branch of the North Anatolian Fault, Western Turkey, *Geophys. J. Int,* **152**(3), 699–717.

Buchanan, D.J., Jackson, P.J. & Davis, R., 1983. Attenuation and anisotropy of channel waves in coal seams, *Geophysics,* **48**(2), 133–147.

Chester, F.M., Evans, J.P. & Biegel, R.L., 1993. Internal structure and weakening mechanisms of the San Andreas Fault, *J. geophys. Res.,* **98**(B1), 771–786.

Cochran, E. & Vidale, J.E., 2001. Seismic anisotropy of the Hector Mine fault zone, in *EOS, Trans. Am. geophys. Un.,* **82,** S41A.

Cochran, E.S., Li, Y.-G., Shearer, P.M., Barbot, S., Fialko, Y. & Vidale, J.E., 2009. Seismic and geodetic evidence for extensive, long-lived fault damage zones, *Geology,* **37**(4), 315–318.

Cohen, G., Joly, P. & Tordjman, N., 1993. Construction and analysis of higher order finite elements with mass lumping for the wave equation, in *2nd Int. Conf. on Mathematical and Numerical Aspects of Wave Propagation,* pp. 152–160, SIAM, Philadelphia.

Eccles, J., Gulley, A., Malin, P., Boese, C., Sutherland, R., Townend, J. & Sutherland, R., 2015. Fault Zone Guided Waves generation on the locked, late interseismic Alpine Fault, New Zealand, *Geophys. Res. Lett.,* **42**(14), 5736–5743.

Ellsworth, W.L. & Malin, P.E., 2011. Deep rock damage in the San Andreas Fault revealed by P- and S-type fault-zone-guided waves, *Geol. Soc. Lond. Spec. Publ.,* **359**(1), 39–53.

Engquist, B. & Majda, A., 1977. Absorbing boundary conditions for the numerical simulation of waves, *Math. Comput.,* **31**(139), 629–651.

Faulkner, D., Jackson, C., Lunn, R., Schlische, R., Shipton, Z., Wibberley, C. & Withjack, M., 2010. A review of recent developments concerning the structure, mechanics and fluid flow properties of fault zones, *J. Struct. Geol.,* **32**(11), 1557–1575.

Golub, G.H. & Loan, C.F.V., 2013. *Matrix Computations,* 4th edn, The Johns Hopkins University Press.

Graves, R.W., 1996. Simulating seismic wave propagation in 3D elastic media using staggered-grid finite differences, *Bull. seism. Soc. Am.,* **86**(4), 1091–1106.

Gulley, A.K., 2017. Computational apapproach for estimating fault-zone properties using trapped waves, *PhD thesis,* The Univercity of Auckland.

Gulley, A.K., Eccles, J.D., Kaipio, J.P. & Malin, P.E., 2017. The effect of gradational velocities and anisotropy on fault-zone trapped waves, *Geophys. J. Int.,* in press, doi:10.1093/gji/ggx200.

Haberland, C. *et al.,* 2003. Modeling of seismic guided waves at the Dead Sea Transform, *J. geophys. Res.,* **108,**(B7), 2342, doi:10.1029/2002JB002309.

Haberland, C. *et al.*, 2007. Shallow architecture of the Wadi Araba Fault (Dead Sea Transform) from high-resolution seismic investigations, *Tectonophysics,* **432**(1–4), 37–50.

Haskell, N.A., 1953. The dispersion of surface waves on multilayered media, *Bull. seism. Soc. Am.,* **43,** 17–34.

Hough, S.E., Ben-Zion, Y. & Leary, P., 1994. Fault-zone waves observed at the southern Joshua Tree earthquake rupture zone, *Bull. seism. Soc. Am.,* **84**(3), 761–767.

Huang, B.-S., Teng, T.-l. & Yeh, Y.T., 1995. Numerical modeling of fault-zone trapped waves: Acoustic case, *Bull. seism. Soc. Am.,* **85**(6), 1711–1717.

Igel, H., Ben-Zion, Y. & Leary, P.C., 1997. Simulation of *SH-* and *P-SV*-wave propagation in fault zones, *Geophys. J. Int,* **128**(3), 533–546.

Igel, H., Jahnke, G. & Ben-Zion, Y., 2002. Numerical simulation of fault zone guided waves: accuracy and 3-D effects, *Pure appl. Geophys.,* **159**(9), 2067–2083.

Jahnke, G., Igel, H. & Ben-Zion, Y., 2006. Three-dimensional calculations of fault-zone-guided waves in various irregular structures, *Geophys. J. Int.,* **151,** 416–426.

Komatitsch, D. & Tromp, J., 1999. Introduction to the spectral element method for three-dimensional seismic wave propagation, *Geophys. J. Int.,* **139**(3), 806–822.

Komatitsch, D. & Tromp, J., 2003. A perfectly matched layer absorbing boundary condition for the second-order seismic wave equation, *Geophys. J. Int.,* **154**(1), 146–153.

Leary, P.C., Li, Y.-G. & Aki, K., 1985. Borehole observations of fault zone trapped waves, Oroville, CA, in *EOS, Trans. Am. geophys. Un.,* **66,** 976.

Leary, P.C., Li, Y.-G. & Aki, K., 1987. Observation and modelling of fault-zone fracture seismic anisotropy–I. *P*, *SV* and *SH* travel times, *Geophys. J. R. astr. Soc.,* **91**(2), 461–484.

Lewis, M., Peng, Z., Ben-Zion, Y. & Vernon, F., 2005. Shallow seismic trapping structure in the San Jacinto fault zone near Anza, California, *Geophys. J. Int.,* **162**(3), 867–881.

Lewis, M.A., Ben-Zion, Y. & McGuire, J.J., 2007. Imaging the deep structure of the San Andreas Fault south of Hollister with joint analysis of fault zone head and direct *P* arrivals, *Geophys. J. Int.,* **169**(3), 1028–1042.

Li, Y.-G. & Leary, P., 1990. Fault zone seismic trapped waves, *Bull. seism. Soc. Am.,* **80,** 1245–1271.

Li, Y.-G. & Vidale, J.E., 1996. Low-velocity fault-zone guided waves: numerical investigations of trapping efficiency, *Bull. seism. Soc. Am.,* **86,** 371–378.

Li, Y.-G. & Vernon, F., 2001. Characterization of the San Jacinto fault zone near Anza, California, by fault zone trapped waves, *J. geophys. Res.,* **106**(B12), 30 671–30 688.

Li, Y.-G. & Malin, P.E., 2008. San Andreas Fault damage at SAFOD viewed with fault-guided waves, *Geophys. Res. Lett.,* **35,** L08304, doi:10.1029/2007GL032924.

Li, Y.-G., Leary, P.C. & Aki, K., 1987. Observation and modelling of fault-zone fracture seismic anisotropy–II. *P*-wave polarization anomalies, *Geophys. J. R. astr. Soc.,* **91,** 485–492.

Li, Y.-G., Leary, P., Aki, K. & Malin, P., 1990. Seismic trapped modes in the Oroville and San Andreas fault zones, *Science,* **249**(4970), 763–766.

Li, Y.-G., Ellsworth, W.L., Thurber, C.H., Malin, P.E. & Aki, K., 1997. Fault-zone guided waves from explosions in the San Andreas Fault at Parkfield and Cienega Valley, California, *Bull. seism. Soc. Am.,* **87**(1), 210–221.

Li, Y.-G., Aki, K., Vidale, J.E. & Alvarez, M.G., 1998. A delineation of the Nojima Fault ruptured in the M7.2 Kobe, Japan, earthquake of 1995 using fault zone trapped waves, *J. geophys. Res.,* **103**(B4), 7247–7263.

Li, Y.-G., Aki, K., Vidale, J. & Xu, F., 1999. Shallow structure of the Landers fault zone from explosion-generated trapped waves, *J. geophys. Res.,* **104**(B9), 20 257–20 275.

Li, Y.-G., Vidale, J., Aki, K. & Xu, F., 2000. Depth-dependent structure of the Landers fault zone from trapped waves generated by aftershocks, *J. geophys. Res.,* **105**(B3), 6237–6254.

Li, Y.-G., Vidale, J., Oglesby, D., Day, S. & Cochran, E., 2003. Multiple-fault rupture of the M7.1 Hector Mine, California, earthquake from fault zone trapped waves, *J. geophys. Res.,* **108**(B3), 2165, doi:10.1029/2001JB001456.

Li, Y.-G., Malin, P.E. & Cochran, E.S., 2012. Fault-zone trapped waves: high-resolution characterization of the damage zone of the Parkfield San Andreas Fault at depth, in *Imaging, Modeling and Assimilation in Seismology,* vol. V1, pp. 107–150, De Gruyter.

Li, Y.-G., Pascale, G.P.D., Quigley, M.C. & Gravley, D.M., 2014. Fault damage zones of the M7.1 Darfield and M6.3 Christchurch earthquakes characterized by fault-zone trapped waves, *Tectonophysics,* **618**(0), 79–101.

Lou, M. & Crampin, S., 1991. Dispersion of guided waves in thin anisotropic waveguides, *Geophys. J. Int.,* **107**(3), 545–555.

Malin, P.E. & Lou, M., 1996. FR waves: A second fault-guided mode with implications for fault property studies, *Geophys. Res. Lett.,* **23**(24), 3547–3550.

Mamada, Y., Kuwahara, Y., Ito, H. & Takenaka, H., 2002. 3-D finite-difference simulation of seismic fault zone waves; application to the fault zone structure of the Mozumi-Sukenobu Fault, central Japan, *Earth Planets Space,* **54**(11), 1055–1058.

Mamada, Y., Kuwahara, Y., Ito, H. & Takenaka, H., 2004. Discontinuity of the Mozumi-Sukenobu Fault low-velocity zone, central Japan, inferred from 3-D finite-difference simulation of fault zone waves excited by explosive sources, *Tectonophysics,* **378**(3–4), 209–222.

Mizuno, T., Nishigami, K., Ito, H. & Kuwahara, Y., 2004. Deep structure of the Mozumi-Sukenobu Fault, central Japan, estimated from the subsurface array observation of fault zone trapped waves, *Geophys. J. Int.,* **159**(2), 622–642.

Mooney, W. & Ginzburg, A., 1986. Seismic measurements of the internal properties of fault zones, *Pure appl. Geophys.,* **124**(1–2), 141–157.

Newmark, N.M., 1959. A method of computation for structural dynamics, *J. Eng. Mech.,* **85**(EM3), 67–94.

Noh, G., Ham, S. & Bathe, K.-J., 2013. Performance of an implicit time integration scheme in the analysis of wave propagations, *Comput. Struct.,* **123,** 93–105.

Peng, Z. & Gomberg, J., 2010. An integrated perspective of the continuum between earthquakes and slow-slip phenomena, *Nat. Geosci.,* **2**(9), 599–607.

Pozrikidis, C., 2005. *Introduction to Finite and Spectral Element Methods using MATLAB,* Chapman and Hall/CRC.

Thomsen, L., 1986. Weak elastic anisotropy, *Geophysics,* **51**(10), 1954–1966.

Thomson, W.T., 1950. Transmission of elastic waves through a stratified solid medium, *J. Appl. Phys.,* **21**(2), 89–93.

Wiggins, R.A., 1976. A fast, new computational algorithm for free oscillations and surface waves, *Geophys. J. Int,* **47**(1), 135–150.

Wu, J. & Hole, J.A., 2011. Refraction of fault-zone guided seismic waves, *Bull. seism. Soc. Am.,* **101**(4), 1674–1682.

Wu, J., Hole, J.A. & Snoke, J.A., 2010. Fault zone structure at depth from differential dispersion of seismic guided waves: evidence for a deep waveguide on the San Andreas Fault, *Geophys. J. Int,* **182**(1), 343–354.